Acta Astronautica 220 (2024) 173–184

Contents lists available at ScienceDirect

Acta Astronautica

journal homepage: www.elsevier.com/locate/actaastro

Test characterization of infrared phototransistors-based sensors for close-proximity operations

Mattia Peruffo [a,*], Alex Caon [a], Francesco Branz [b], Alessandro Francesconi [b]

[a] Centre of Studies and Activities for Space (CISAS) "Giuseppe Colombo", University of Padua, via Venezia, 15, Padua, 35131, Italy
[b] Department of Industrial Engineering, University of Padua, via Venezia, 1, Padua, 35131, Italy

ARTICLE INFO

Keywords:
Modular assembly
Testing campaign
Capture interface
Navigation sensors
AUTOMA

ABSTRACT

On-orbit servicing and on-orbit assembly represent very appealing mission concepts that could facilitate the exploitation of the space environment. Autonomy is a critical requirement for systems aimed at the execution of these operations. The development of enabling technologies for this type of missions is a focal research topic for the global space community. The AUTOMA project (University of Padua, Italy) aims at the development of technologies to enable the on-orbit assembly of a standardized modular unit by means of a robotic arm. The goal is the development of a capture interface, composed of a gripper mechanism and a suite of close-range navigation sensors (a navcam, four time-of-flight sensors, two custom matrix sensors based on a set of phototransistors), and the mock-up of a modular assembly unit. The paper prevalently focuses on the conspicuous series of tests that has been performed at subsystem level for the characterization of the two custom matrix sensors, both in terms of their resolution and range of application. In particular, the test campaign has proven how the in-plane matrix sensor provides information about lateral misalignment and relative distance with a resolution of a few millimetres while the roll matrix sensor provides information about the angular roll misalignment with a resolution dependent on the distance between the two bodies. In addition, an analytical relation for the computation of the relative distance through the information provided by the in-plane matrix has been investigated.

1. Introduction

Very promising and engaging space mission concepts for both the industrial and the scientific community have recently acquired a prominent interest. *On-Orbit Servicing* (OOS) missions comprise a series of operations [1,2] (such as, for instance, inspection, refuelling and refurbishing) aimed at the extension of the operational life or the safe disposal of the satellite. *On-Orbit Assembly* (OOA) missions foresee the building of large structures (antennas, telescopes and solar panels) directly in space often by means of standardized modular units. *Active Debris Removal* (ADR) missions aim at the remediation of the space debris problem by reducing the number of debris (defunct vehicles and/or singular parts of satellites) in orbit. Due to the substantial level of difficulty and critical challenges that characterize these types of mission, both industrial and academic institutions are focusing their studies and efforts on the development of technologies to enable these operations [3–5]. The high degree of autonomy that characterizes these technologies represents a key factor in order to safely execute these critical operations whilst also reducing the errors introduced by human interventions. While two successful OOS missions have already been performed [6,7], only a technology feasibility demonstrative mission has been completed for ADR [8,9], with two real missions scheduled for the near future [10,11]. On the other hand, although several mission designs have been proposed for OOA projects [12–15], only some technology feasibility missions are expected to be planned [16,17], still without a concrete schedule arranged.

In this frame, the Department of Industrial Engineering of the University of Padua is pursuing its research interest on these topics with the project AUTOMA (*AUtonomous Technologies for Orbital servicing and Modular Assembly*). The project aims at the development of technologies (both software and hardware) which could be employed for OOS, OOA and ADR missions. Two distinct mission scenarios have been taken into account, namely an orbital mission scenario and a planetary mission scenario. Although it could seem that the two scenarios considered do not present similarities in terms of application, they share many common technologies that will enable them.

* Corresponding author.
E-mail address: mattia.peruffo@unipd.it (M. Peruffo).

https://doi.org/10.1016/j.actaastro.2024.04.010
Received 29 September 2023; Received in revised form 18 January 2024; Accepted 7 April 2024
Available online 16 April 2024

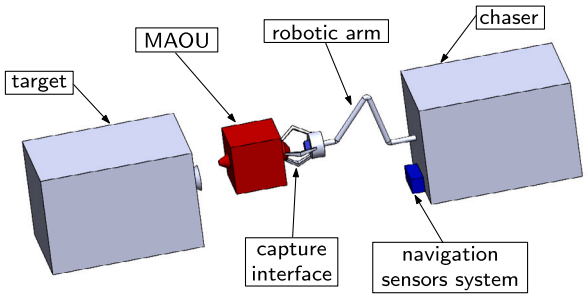

Fig. 1. Schematic representation of the orbital mission scenario.

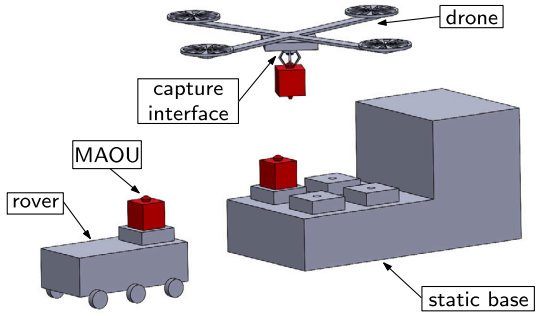

Fig. 2. Schematic representation of the planetary mission scenario.

Orbital mission scenario

The orbital mission scenario (Fig. 1) foresees the participation of two satellites, namely a chaser (equipped with a navigation sensors system and a robotic arm) and a target. The end-effector of the robotic arm consists of a capture interface, composed of both a gripper mechanism and a suite of close-range navigation sensors. The chaser carries some Modular Assembly Orbital Unit(s) (MAOU), a standardized module which provides the additional and/or replacement resources required by the target vehicle. The robotic arm is employed to grab MAOU from its storage and to locate it on the target vehicle, which presents an interface dedicated to the docking operation with MAOU.

Planetary mission scenario

The planetary mission scenario (Fig. 2) foresees the involvement of a series of multiple vehicles, both aerial (drones) and terrestrial (rovers), and static bases which share both data and resources. The vehicles are used to explore the site while the static bases act as stationary scientific laboratories. Thanks to their higher mobility and velocity, the drones can both enhance the exploration capabilities compared to the rovers and easily transport additional resources and/or replacement parts required by other agents of the group. The drone is equipped with a capture interface composed of a gripper mechanism and a suite of close-range navigation sensors. The capture interface is mounted under the drone and it is exploited to move MAOU, which acts either as provider of additional resources to be integrated or as container for scientific samples to be analysed, to the required location.

In order to validate the technologies exploited in the two mission scenarios, the research project has been divided in three experimental scenarios, each one focused on a particular aspect of technology development previously described.

The first experimental scenario (A) foresees the participation of two satellite mock-ups, respectively a controllable chaser and a not cooperative target, in a relative motion over a low-friction table. The scenario focuses on the navigation sensors system, based on a stereo vision camera, mounted on the chaser. In particular, the main objective consists in the evaluation of the performances of a model-based algorithm which determines the relative pose between the two vehicles in a real time application by means of an embedded mini computer.

The second experimental scenario (B) foresees the involvement of a target mock-up free to move on a low-friction table and a six degrees of freedom (DoF) robotic arm. The scenario focuses on both the standardized modular unit MAOU and the capture interface at the end-effector of the robotic arm required to move it. The main objective consists in the evaluation of the assembly feasibility of a standardized modular unit onto the nanosatellite mock-up by means of the robotic arm.

The third experimental scenario (C) foresees the usage of a fixed target mock-up and a drone free to move in a controlled flying arena. The scenario should employ the technologies already developed in the experimental scenario B, namely the standardized modular unit and the gripper mechanism, thus focusing on the integration between the drone and the capture mechanism and their control. The main objective consists in proving the feasibility of automatic assembly and reconfiguration of miniature structures by means of drones.

The work presented in this paper ensues from the activities carried out in the framework of experimental scenarios B and C, involving the development of both the capture interface and the standardized modular unit. The suite of close-range navigation sensors, that constitutes part of the capture interface, comprises two custom sensors internally developed. Although a description of the hardware designed (MAOU and capture interface) is presented, this paper mainly focuses on the test campaign carried out in order to characterize the two custom sensors, both in terms of their resolution and range of application. The remaining part of the paper is organized as follows. After a brief description illustrating the laboratory facility, the design of both the gripper mechanism and the modular unit is introduced in Section 2. Section 3, which reports the main focus of the paper, is dedicated to the test campaign performed at subsystem level aimed at the characterization of the two custom sensors incorporated in the capture interface, with a detailed description of both the experimental setup and the test procedures, followed by the analysis of the main results achieved. Based on the data of the tests, Section 4 focuses on the definition and the comparison of various approaches for the retrieval of a function relation of the axial distance between the gripper mechanism and the standardized modular unit MAOU to be used during its grasping. Finally, in Section 5 conclusions are drawn.

2. Hardware

The experimental scenarios comprising the activities presented in this paper aim at the analysis of the assembly feasibility of a standardized modular unit onto a target mock-up by means of either a robotic arm or a drone. The activities have been carried out in the Space Systems Laboratory of the Department of Industrial Engineering. The research group presents a consolidated heritage in close proximity operations (CPO) technologies, such as docking mechanisms [18,19], GNC systems [20] and relative navigation sensors systems [21]. In addition, the laboratory facility already comprises: a low-friction table, that enables a three DoF motion in a drag-free condition; a six DoF custom robotic arm [22], whose end-effector can be interchanged in order to test different grasping mechanisms; a set of four infrared motion capture cameras,[1] which can provide an accurate reference for the motion of both the robotic arm and the satellite mock-ups. In this framework, the main efforts of the activities related to the project have focused on the hardware involved, respectively the capture interface and the standardized modular unit MAOU, both in terms of design and testing. Due to the heritage of the group in terms of mechanisms, a preliminary prototype form of the capture interface has already been

[1] OptiTrack Prime^x 13.

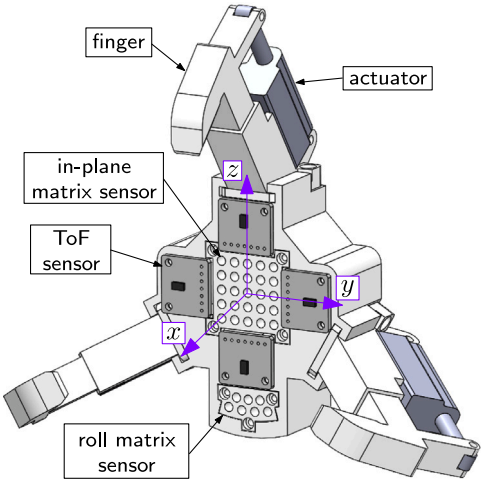

Fig. 3. CAD model of the improved capture interface.

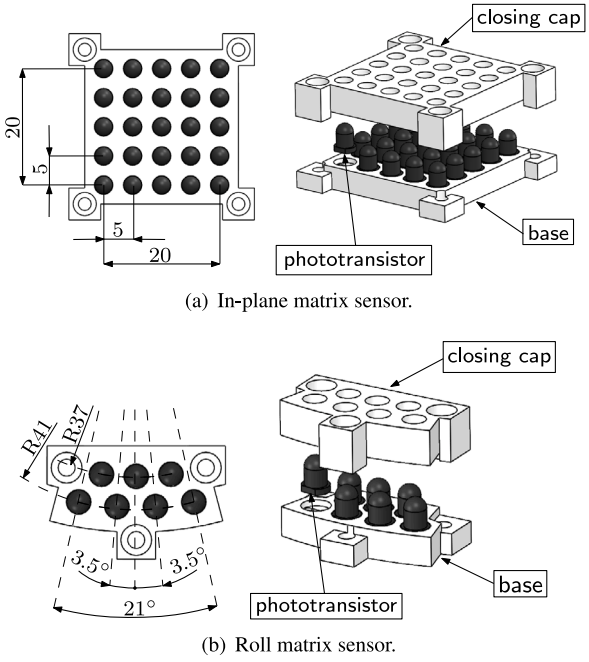

(a) In-plane matrix sensor.

(b) Roll matrix sensor.

Fig. 4. Matrix sensors: front view (left) and exploded view (right).

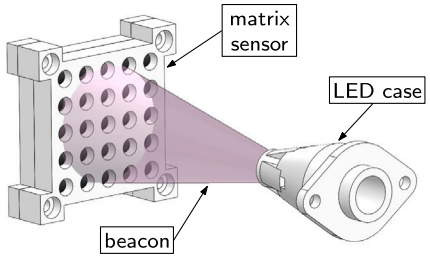

Fig. 5. CAD model of the two coupled parts of the sensor: matrix sensor and infrared LED beacon.

conceived [23] and it has been taken as reference for the subsequent developments. In this section a detailed description of the hardware designs will be presented, while the next section is dedicated to the test campaign performed.

2.1. Capture interface

The prototype capture interface SMACK (*SMArt Capture Kit*) is a smart capture interface composed of both a gripper mechanism and a suite of close-range navigation sensors. The interface has been designed to be an independent set for close-range operations, allowing the retrieval of the relative pose of the target object and performing its capture. The original prototype model has been taken as reference to develop an improved version with additional capabilities. Great relevance has been given to the modularity of the structure of the mechanism, whose elements can be easily separated and modified when required.

The mechanism consists of a central main body and three claws. Each claw can slide inside its case actuated independently through a miniaturized linear actuator (Actuonix PQ12). The suite of sensors is composed of four different types, respectively a navcam,[2] a set of four time-of-flight (ToF) sensors[3] and two customized sensors based on a matrix of phototransistors. With the exception of the navcam, the entire suite of remaining sensors is integrated directly in the main body of the mechanism, as depicted in Fig. 3.

The navcam is part of a self-consistent navigation system package which comprises two patterns of four infrared LEDs each. An exhaustive description of the package can be found in [21]. The navcam can be exploited for distance applications down to 100 mm, while for values below this limit the condition of out of focus of the camera precludes its usage. Additional sensors are required in the near distance range in order to compute the relative pose of the target object. For this reason, a set of four ToF sensors is exploited. With reference to Fig. 3, the ToF sensors are arranged on the yz plane of the main body of the gripper mechanism: ToF_1 and ToF_3 are along the y-axis, respectively on $+y$ and $-y$, while ToF_2 and ToF_4 are along the z-axis, respectively on $+z$ and $-z$. Each ToF sensor presents a distance a from the centre of the main body (i. e. the centre of the reference system) equal to 25 mm. The sensor provides the measurement of distance of the target surface orthogonal to its plane. The range of application of the ToF sensors is between 100 mm and 20 mm. Below the lower boundary limit, the jitter of the sensors tends to considerably affect, and consequently compromise, the distance measurements provided. Due to these limitations, in the very near distance range the suite of four ToF sensors would not be able to provide information about the pose of the target object. Additional measurements are required in order to determine the relative pose of the target object with satisfactory accuracy to perform the capture. For these reasons, two custom matrix sensors are employed in the very near distance range.

Both the matrix sensors share similar building structures (Fig. 4) and working principles (Fig. 5). Each matrix is composed of two main parts: the lower base acts as seat for the phototransistors[4] while the upper cap is used as closing top to avoid their motion. Both the matrix sensors are paired with their own counterpart, an infrared LED source which acts as a beacon for the phototransistors activation. The figure generated by the lit phototransistors is exploited to retrieve part of the relative pose information of the target. The first matrix sensor (in-plane matrix) employs a set of 25 phototransistors equally arranged in a square shape, evenly distributed with a pitch of 5 mm. It provides information about both the lateral displacement with respect to its centre (i. e. the centre of the gripper mechanism) and the axial distance from the target object. The in-plane matrix, as the main sensor to rely on during the very near distance of the approach phase, shall present a range of application up

[2] Raspberry Pi Camera Module v1.

[3] VL6180.

[4] Silicon NPN phototransistor OSRAM SFH 309 FA.

to a minimum distance of 30 mm, in order to partially overlap with the range of application of the ToF sensor. In addition, the matrix sensor shall be characterized by a resolution of 3 mm. The second matrix sensor (roll matrix) employs a set of seven phototransistors arranged on two radii, respectively three on the smaller radius and four on the greater radius, with an angular pitch between consecutive phototransistors of 3.5 deg. It provides information about the angular roll misalignment with respect to the axis of symmetry of the gripper mechanism. As in the case of the in-plane matrix, the roll matrix shall be employed in the very near range distance phase of the approach. Assuming the roll alignment as the last operation before the execution of the docking between the gripper and its target, the sensor shall present a range of application up to a minimum of 20 mm. In addition, considering how the features of the three appendices on MAOU should ease the grasping procedure, the roll matrix shall be characterized by a resolution of 5 deg.

The measurements provided by the several sensors of the suite are exploited to compute the relative pose between the gripper mechanism and its target. In order to improve the retrieval of the relative pose, the measurements are combined with a sensor fusion approach by means of a model-based algorithm, which provides an estimation of the relative pose information. A simplified linear version comprising only the measurements of the suite of four ToF sensors has already been discussed in a previous work [24].

2.2. MAOU

The MAOU unit represents a standardized module aimed at the provision of the resources required by the target vehicle. The unit is equipped with both an interface dedicated to the grasping mechanism which moves MAOU and an interface dedicated to the docking with the target vehicle. Fig. 6 depicts the design of a simplified mock-up version of the unit that has been used for the experimental evaluation. The simplified mock-up is representative of the geometry of a functional unit, while neither the mass nor the volume could characterize a real operative one, since there is no space allocated to the resources that should be provided to the target vehicle. However, its structure is composed of the two main interfaces required for the operations of MAOU. The first interface (gripper interface) is dedicated to the grasping operations of MAOU by means of the gripper mechanism. It presents three appendices, which act as grasping location for the claws of the gripper mechanism, and it is equipped with two cases for the infrared beacon LEDs, the counterpart sources for the matrix sensors. The second interface (docking interface) is dedicated to the docking operations of MAOU with the target vehicle. The docking mechanism employed is of a probe-drogue type [19]. The conic shape of the probe allows the self-alignment during the insertion phase. At the condition of full insertion detected by the fork sensor, the tip of the probe rotates and rigidly connects the probe and the drogue, thus completing the docking manoeuvre.

3. Test campaign

A conspicuous series of tests has been carried out in order to evaluate the performances of the capture interface, both at subsystem and system level. This section focuses on the tests performed to characterize the two matrix sensors, while a detailed description of the test campaign aimed at the assessment of the whole sensor package can be found in [25].

The experimental setup, employed for the characterization of both the matrix sensors, consists of a linear slide which can provide up to three DoF (Fig. 7). The moving part of the slide is attached to two motorized threaded rods, perpendicular to each other, which enable the two translational DoF on the xy-plane. Instead, a motorized unit mounted on top of the moving part provides the third DoF, enabling the rotation along the z-axis. The motion is provided by stepper motors integrated with their own encoders which give a reference measurement of the imposed movement.

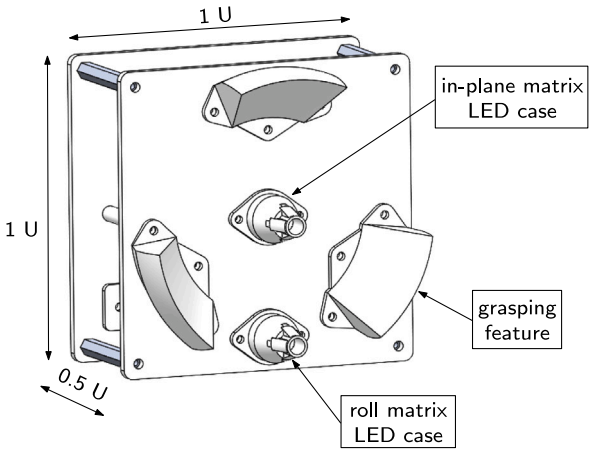

(a) Gripper interface.

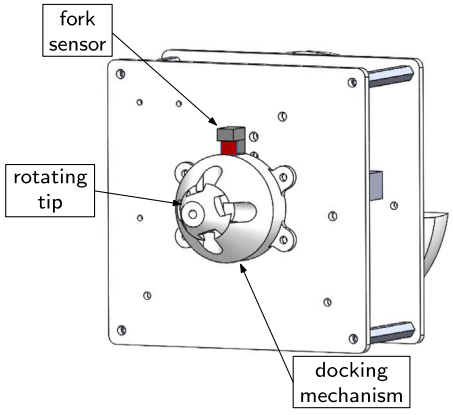

(b) Docking interface.

Fig. 6. CAD model of MAOU.

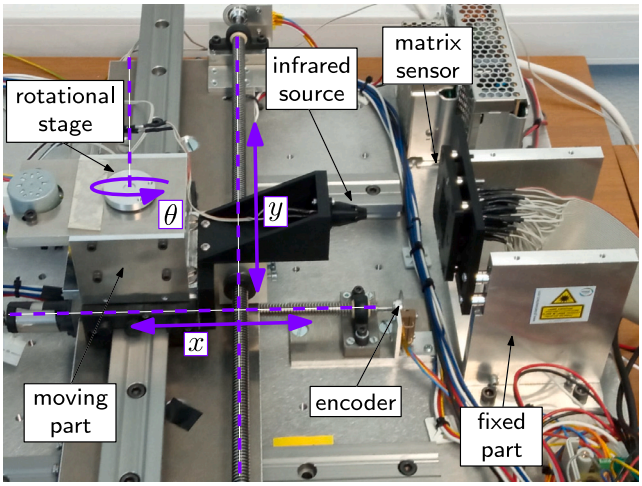

Fig. 7. Experimental setup employed for the characterization tests of the matrix sensors.

3.1. In-plane matrix

The in-plane matrix has already been developed by the authors as part of the close-range navigation sensors suite of the SMACK prototype [23]. The original design of the sensor foresees the usage

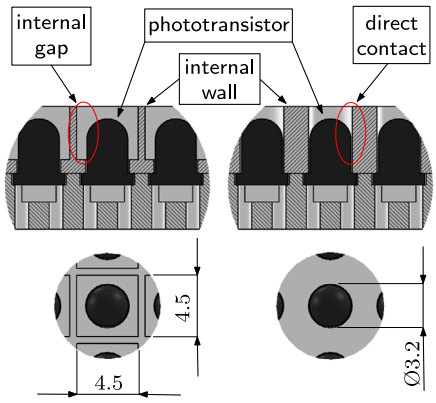

Fig. 8. Detail of the closing caps of the in-plane matrix: cap A (on the left) and cap B (on the right).

of a closing cap characterized by square-shaped holes and an infrared LED beacon with an angular aperture of 17 deg. A preliminary characterization of the original design of the sensor can be found in [26].

In the framework of the AUTOMA project, a more extensive analysis of the sensor features has been executed, employing LEDs with different angular aperture and evaluating the contribution of the dimension of the closing cap openings to the performance of the sensor. In particular, two different types of closing cap have been taken into account, as depicted in Fig. 8. The former (cap A) is equal to the original design and it presents square-shaped holes with a gap between the internal wall of the opening and the external side of the phototransistor, whereas the latter (cap B) presents circular-shaped holes whose internal wall is directly in contact with the phototransistor. Maintaining a separation wall between consecutive phototransistors, the two cap configurations selected can be thought as the two boundary designs. In fact, cap A allows the maximum gap between its internal wall and the phototransistor. On the other hand, cap B reduces to the minimum the gap between its internal wall and the phototransistor. Therefore, while cap A represents the original design already developed, cap B has been chosen as alternative configuration and possible improvement to be evaluated. Each phototransistor is characterized by a frontal cone of sight that determines the activation of its chip. In the case of cap A, the gap of the openings internal walls does not influence the cone of sight of the phototransistor, enabling its trigger by both straight perpendicular and inclined infrared beams. On the other hand, the direct contact of the internal walls of the cap B openings narrows the cone of sight of the phototransistor, thus restricting its activation only by means of straight orthogonal infrared rays.

Theoretically, the behaviour of the two closing cap configurations in combination with the infrared LED counterpart could be assessed by means of a numerical simulation purely based on a geometrical approach. However, the definition of the geometries related to both the main emission lobe of the infrared LED and the cone of sight of the phototransistors would be approximate and not completely representative of their actual behaviour. In addition, a simulation purely based on geometrical aspects would not be able to take into account additional secondary effects, such as internal wall reflections, thus leading to an unrealistic estimate of the sensor behaviour. As reported in [26] for the original design of the in-plane matrix, the characterization by means of an experimental procedure results more exhaustive as opposed to the one by means of a pure geometrical approach, since the simulation overlooks some aspects which are instead present in the experimental procedure. For this reason, in order to properly describe the sensor response, an experimental characterization has been selected.

Two typologies of tests have been carried out. In both cases, the matrix sensor has been located on the fixed part of the rail while the infrared LED source has been mounted on the moving part.

Table 1
Lateral resolution of the in-plane matrix [mm].

	cap A	cap B
res_{lat}	2.00	3.00

3.1.1. Lateral displacement test

The first type of tests has aimed at the definition of the lateral characterization of the sensor in terms of resolution. The LED has been placed on the moving part of the rail, mounted perpendicular to the in-plane matrix surface at a distance of 25 mm, and a fixed-step motion along the y direction has been imposed. Due to the condition of constant distance, the radius of the projected circle (resulting from the intersection between the infrared beam and the plane of the sensor) does not change during the motion imposed. For this reason, only one type of infrared LED[5] with an half angular aperture of 10 deg has been employed. Considering the alignment between the LED and the central phototransistor as the condition of null misalignment, the infrared source has been moved to consecutive positions along the y direction inside the range $[-15, 15]$ mm. Several imposed steps Δy have been employed:

$$\Delta y = 0.5i \quad \text{with} \quad i = 1, \dots, 10 \tag{1}$$

where the value of Δy is expressed in mm. For each step considered, a total amount of five test repetitions has been executed. The motion of the LED along the y direction determines which phototransistors activate. The pattern of these is identified by the position of its centroid, computed through the mean of the positions of lit phototransistors, with respect to the centre of the sensor. The change of the pattern between consecutive movements determines the level of lateral resolution of the sensor. In fact, the lateral resolution has been defined as the minimum fixed step for which there is a variation of the pattern of activated phototransistors at every movement imposed. Table 1 reports the main results of the test campaign. The table points out how both the configurations are compliant, in the lateral motion, with the resolution requirement imposed. Nonetheless, the table highlights how the cap A provides a better lateral resolution compared to the cap B. In fact, the cap A, whose wider square-shaped openings do not strictly enclose the chip of the phototransistor, requires a lower fixed-step motion for a pattern change of the activated phototransistors.

3.1.2. Axial displacement tests

The second type of tests has focused on the axial characterization of the sensor, in terms of both upper boundary limit of application and resolution. The infrared source has been placed on the moving part of the rail and a fixed step motion Δx of 1 mm along the x direction has been imposed. The infrared source has been shifted from an initial condition of null distance from the surface of the in-plane matrix up to a maximum distance of 100 mm. The variation of distance between the LED and the matrix sensor affects the size of the radius of the projected circle on the plane of the matrix, thus consequently having an impact on the number N of phototransistors activated. The pattern ranges from a minimum condition of the single central active phototransistor ($N = 1$) to a maximum condition of the whole set of active phototransistors ($N = 25$). An example of a series of pattern change is reported in Fig. 9. As opposed to the lateral displacement test type, in this case the influence of the infrared source has been investigated. In fact, for the same relative distance between the LED and the matrix sensor, the dimension of the projected circle is affected by the angular aperture of the beacon, thus consequently having an impact on the number N of activated phototransistors. In particular, a greater angular aperture corresponds to a wider dimension of the projected circle. Considering

[5] Infrared emitter OSRAM SFH 4544.

Table 2
Range of application in axial direction of the in-plane matrix [mm].

	cap A	cap B
LED_3	0 ÷ 45	0 ÷ 50
LED_5	0 ÷ 39	0 ÷ 50
LED_{10}	0 ÷ 36	0 ÷ 49
LED_{17}	0 ÷ 56	0 ÷ 59

that during the motion of the infrared source in the axial displacement tests the dimension of the projected circle tends to change, the angular aperture of the beacon represents a parameter to be taken into account for the analysis of the sensor performances. For this reason, a selection of the LEDs to be employed has been required. Although several LEDs were taken into account, a shortlisted selection has been effectively defined, predominantly considering the angular aperture and the market availability as main drivers. Among the ones available on the market, a list of three LEDs from the same manufacturer has been selected. The shortlisted set shares comparable characteristics in terms of radiation intensity and each LED is characterized by a different value of half angular aperture, namely 3 deg (LED_3),[6] 5 deg (LED_5)[7] and 10 deg (LED_{10}).[8] In addition, a fourth LED characterized by an half angular aperture of 17 deg (LED_{17})[9] has been employed. Compared to the others, this LED presents different characteristics both in terms of manufacturer and radiation intensity. However, it has been employed anyway due to analysis considerations for the comparison of relations for the retrieval of the axial distance x by means of the information provided by the in-plane matrix, as reported in Section 4. For each LED employed, a total amount of 10 test repetitions has been executed.

The variation in the pattern of phototransistors activated with respect to the distance between the LED and the matrix sensor has been exploited in order to compute both the upper boundary limit of application and the axial resolution.

The upper boundary limit of application has been defined as the minimum distance at which the maximum amount of activated phototransistors occurs. Table 2 summarizes the ranges of application of the sensor, in reference to both the type of LED considered and the closing cap employed. Some interesting considerations can been inferred. First, overall an increase of the half aperture angle of the LED corresponds to a reduction of the range of application of the sensor. In fact, the radius of the projected circle on the sensor plane is affected by the angular aperture of the infrared beam. For a fixed axial distance, a narrower angular aperture is equivalent to a lower radius dimension and consequently to a minor amount of phototransistors inside the projected circle, condition that determines their activation. For this reason, the trigger of the whole set of phototransistors occurs at a greater distance for LEDs characterized by a lower angular aperture. The different trend followed by LED_{17} could result from its different characteristics compared to the others in terms of power dissipations and radiant intensity. Second, the usage of the cap B determines an improvement of the upper boundary limit of the sensor compared to cap A. The cause of this behaviour can be attributed to the reduced cone of sight of the phototransistors in the case of cap B. This characteristic affects the occurrence of activation of the phototransistors, especially those located on the more perimetral part of the matrix sensor. For this reason, the infrared source needs to be positioned at a greater distance, as opposed to the case of usage of cap A, in order to enable the activation of the whole set of phototransistors. Nonetheless, both configurations are compliant with the required range of application.

[6] Infrared emitter OSRAM SFH 4550.
[7] Infrared emitter OSRAM SFH 4545.
[8] Infrared emitter OSRAM SFH 4544.
[9] Infrared emitter Kingbright L-7104F3C.

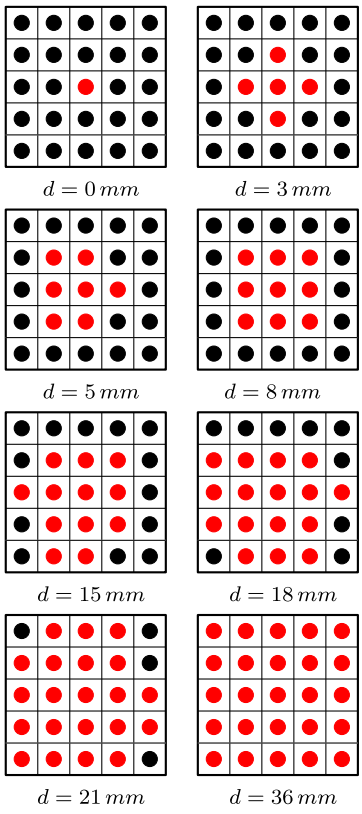

Fig. 9. Example of pattern variation with respect to the axial distance d: active phototransistors are in red while not active phototransistors are in black. The data reported refer to a test iteration employing cap A on the matrix sensor side and an half angular aperture of 10 deg beam on the LED side. (For interpretation of the references to colour in this figure legend, the reader is referred to the web version of this article.)

Table 3
Axial resolution of the in-plane matrix [mm].

	cap A	cap B
res_{ax}	2.5	3.0

With reference to the axial resolution of the sensor, the results are collected in Table 3. As in the case of the lateral test campaign, the table points out how both configurations are compliant in the axial direction with the resolution requirement imposed. Similarly to the lateral motion, the table highlights how the cap A, with its wider square-shaped openings, provides a better axial resolution compared to the cap B. In addition, the values reported in Tables 1 and 3 indicate, for both configurations, a slightly better resolution in the lateral direction compared to the one in the axial direction.

Furthermore, although both the closing caps present a similar trend in terms of variation frequency of the pattern of activated phototransistors, cap A seems to be characterized by a finer sensibility in the very close range, as depicted in Fig. 10.

In reference to the application case study considered (capture of MAOU), since the in-plane matrix represents the main sensor of the suite to rely on during the nearest phase of the capture, the cap A seems the most suitable thanks to its improved resolution, both in the lateral and axial directions. With respect to this consideration and keeping in mind the range requirement, on the infrared source side either LED_5 or LED_{10} represent the most valid candidates to be employed. Their similar ranges of application are compliant with the requirement imposed and do not excessively surpass the inferior limit of the ToF sensor, over which the ToF represents the main sensor for

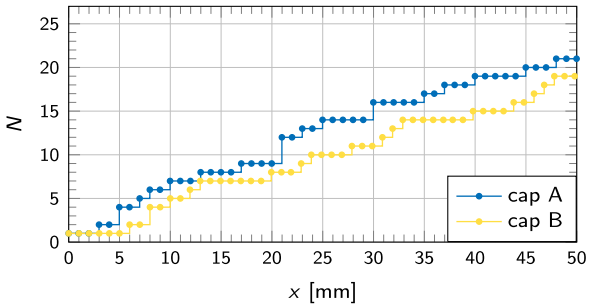

Fig. 10. Comparison of the axial sensitivities of the closing caps of the in-plane matrix in terms of activated phototransistors pattern change.

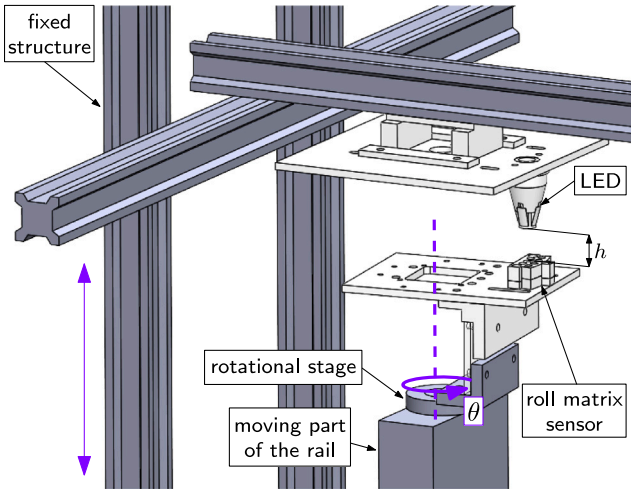

Fig. 11. Schematic CAD model of the test facility employed for the characterization of the roll matrix sensor.

pose estimation to rely on thanks to its characteristics. An increase of the range of application of the in-plane matrix sensor (and consequently the overlapping between the ranges of ToF and matrix sensors) would not provide a significant improvement. On the contrary, the reduction of the angular aperture of the LED, required by the increase of the application range, could be disadvantageous in the case of not optimal orthogonality between the infrared beam and the surface of the sensor.

3.2. Roll matrix

Since the roll matrix is a sensor entirely developed in the framework of the AUTOMA project, the test campaign carried out in this work has aimed at a complete characterization focusing on the definition of its resolution, its range of application and the measurement errors provided.

For the execution of the test campaign, the sensor has been located on the rotational stage on the top of the moving part of the rail while the LED source has been mounted on a fixed structure over the sensor specifically designed for the tests to be performed, as depicted schematically in Fig. 11. The structure not only keeps the infrared source in a condition of orthogonality with respect to the surface of the roll sensor, but it also maintains their distance constant during the execution of the test iteration. In addition, the structure has been designed with the capability to enable the adjustment of the relative distance h between the LED and the sensor in order to evaluate its influence on the sensor performance. A total amount of 10 values has been considered:

$$h = 5i \quad \text{with} \quad i = 1, \dots, 10 \tag{2}$$

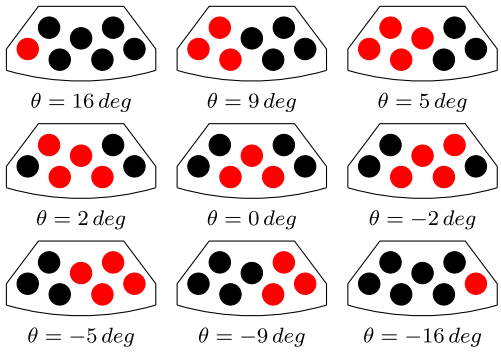

Fig. 12. Example of pattern variation with respect to the angular misalignment θ: active phototransistors are in red while not active phototransistors are in black. The data reported refer to a test iteration executed at a distance h of 5 mm. (For interpretation of the references to colour in this figure legend, the reader is referred to the web version of this article.)

where the distance h is expressed in mm. Considering the alignment between the LED and the axis of symmetry of the roll sensor as the condition of null misalignment, an angular motion in the range $[-20, 20]$ deg has been imposed to the rotational stage, with a fixed angular step $\Delta\theta$ of 1 deg. The same procedure has been applied to the whole set of distances h considered. For each distance value, a total amount of five repetitions has been executed. The imposed angular motion determines a variation of the pattern of phototransistors activated by the infrared source. An example is reported in Fig. 12. Each pattern is identified by the angular position of its centroid, computed through the mean of the positions of lit phototransistors, with respect to the axis of symmetry of the sensor. The position of this pattern is exploited to retrieve the information of relative angular misalignment between the LED and the sensor.

Considering the close proximity of the phototransistors to each other (Fig. 4), on the source side it has been decided to employ only one LED[10] with an half angular aperture of 3 deg while on the sensor side the closing cap B has been chosen to be used. The angular aperture of the LED directly affects the radius dimension of the projected circle of the beam on the sensor surface: a minor angular aperture corresponds to a lower value of the radius. The usage of cap B narrows the cone of sight of phototransistors. These conditions favour both an increase of the distance range h at which the sensor can be employed and a better identification of pattern variation between diverse angular positions.

Fig. 13 depicts an example of the data collected from one of the test iterations carried out. The upper graph illustrates a comparison between the values of the angular position imposed by the motorized stage (provided by the encoder) and the values of angular misalignment computed from the pattern of activated phototransistors. Overall, the graph suggests how the sensor results active even for angular positions outside its theoretical geometric range of application of ± 10.5 deg. In case none of the phototransistors is activated the sensor is not able to provide an angular information. This fact is more noticeable the lower is the value of relative distance h. The second plot reports, for each angular position, the absolute error between the values measured by the encoder and those computed by the roll matrix, respectively. The chart not only outlines the symmetric behaviour of the sensor, but it also highlights how the discrepancy between the angular values compared tends to rise with the increase of angular misalignment between the LED and the sensor.

The test campaign has also provided interesting results regarding the influence of the relative distance h on the performances of the sensor. The value of h directly affects the radius of the projected circle

[10] Infrared emitter OSRAM SFH 4550.

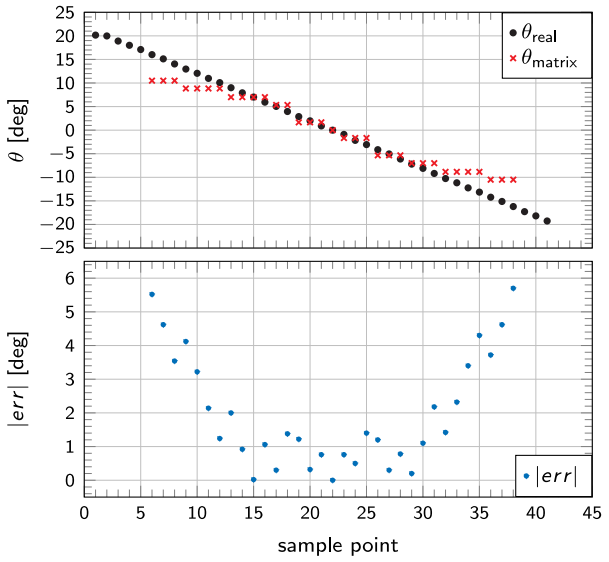

Fig. 13. A sample of the roll matrix tests ($h = 5$ mm): comparison between the imposed and computed angular displacement (above); absolute error between the imposed and computed angular displacement (below).

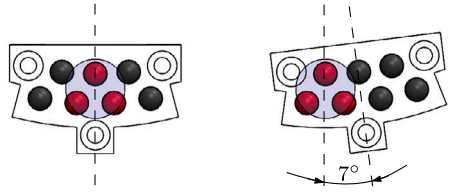

(a) $h = 5$ mm: the matrix sensor provides the measurements of 0 deg and 7 deg, respectively in the case of alignment and misalignment.

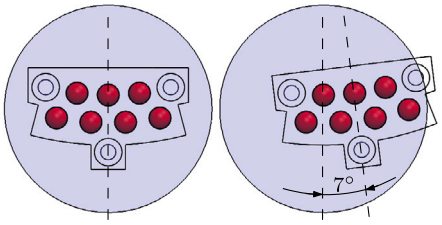

(b) $h = 50$ mm: the matrix sensor provides the measurements of 0 deg in both the case of alignment and misalignment.

Fig. 14. Comparison of phototransistors activation pattern between $h = 5$ mm and $h = 50$ mm in an imposed condition of alignment ($\theta = 0$ deg) (left) and misalignment ($\theta = 7$ deg) (right).

on the surface of the matrix: the farther the LED is from the sensor, the greater the size of the radius. The dimension of the projected circle determines which phototransistors are activated by the infrared source, thus affecting the measurement provided by the roll matrix sensor. Fig. 14 depicts a schematic visualization of the phenomenon presented. A comparison between a condition of alignment and misalignment is reported for two distance values of the range considered, namely at $h = 5$ mm and at $h = 50$ mm. In the case of very near proximity (Fig. 14(a)), the restricted size of the projected circle allows the sensor to provide different measurements between the two conditions imposed thanks to a change of the pattern of active phototransistors. On the other hand, at a greater distance (Fig. 14(b)) the size of the projected circle determines the activation of the whole set of phototransistors in both the two conditions imposed, preventing their distinction. Therefore, the relative distance h has an impact on the level of resolution of the sensor. Table 4 reports the values of angular resolution in reference to h. The results are collected for distance ranges. The table highlights how the roll sensor satisfies the resolution requirement imposed only for a subset of distances h tested. Nonetheless, this subset is compliant with the application range requirement defined, considering the exploitation of the roll sensor in the last phases of the grasping manoeuvre.

Table 4
Angular resolution of the roll matrix.

h range [mm]	Resolution [deg]
5.0 ÷ 20.0	3.5
25.0 ÷ 30.0	5.0
35.0 ÷ 50.0	6.5

Table 5
Average and standard deviation of the absolute error between imposed and computed angular positions.

h [mm]	avg [deg]	σ [deg]
5	2.05	1.67
10	2.66	2.19
15	3.65	2.47
20	4.50	2.74
25	5.11	2.84
30	6.03	3.29
35	6.51	3.40
40	6.82	3.36
45	7.00	3.41
50	7.21	3.74

In terms of sensor activation, a greater relative distance h involves a wider angular range of application. In fact, the larger size dimension of the projected circle, corresponding to a greater value of h, allows the activation of the most external phototransistor at a broader maximum angular position of misalignment. However, as stated previously in reference to Fig. 13, since the maximum measurement value provided by the sensor is 10.5 deg (angular position of the outer singular phototransistor), the discrepancy between the imposed and computed angular values tends to increase with the extension of the angular misalignment. In addition, as pointed out in Fig. 14(b), the greater size of the projected circle can prevent the identification of a condition of misalignment, thus increasing the errors provided by the sensor. This fact is more noticeable for angular positions in a neighbourhood of the condition of alignment. Table 5 compares the values of average and standard deviation of the absolute error between the imposed and computed angular positions in the restricted angular range taken into account. The results are reported in reference to the value of h considered. The table suggests how the roll matrix exploitation should be limited to the last phases of the grasping manoeuvre. In fact, the greater proximity between the roll sensor and the infrared beacon corresponds to a lower angular measurement error. The application range requirement supports this choice.

4. Axial distance retrieval comparison

The previous section has presented the test campaign carried out to characterize the two custom sensors. Focusing on the in-plane matrix sensor, Section 3.1.2 has pointed out how the pattern of active phototransistors is influenced by the distance from the infrared source. In order to retrieve the axial distance x between the gripper mechanism and MAOU by means of the information provided by the in-plane matrix sensor (the number of phototransistors activated N), a relation between x and N is required. Although the authors have already provided an example of such relation in [23], it is based on a fuzzy

logic inference system with a "qualitative" if-then rule approach. The current work has focused on the definition of an analytical relation between x and N, by means of the identification of a fitting curve[11] from a set of sample points of the type (N, x). In order to make a direct comparison with the fuzzy logic methodology already developed, the data provided by the test campaign involving LED_{17} (on the source side) and the closing cap A (on the sensor side) have been employed as set of sample points. Only the data which present a relative distance lower than the threshold value $x_{\mathrm{thresh}} = 50$ mm have been considered in the dataset. For the definition of the relation between x and N, three different approaches have been examined.

In the first case, a regression model parametric fitting approach has been employed. The function model selected assumes a polynomial form

$$\mathrm{poly}_m : \; x = \sum_{i=0}^{m} a_i N^{m-i} \tag{3}$$

where a_i represents the coefficients of the polynomial of degree m. Polynomials up to the 9th degree have been taken into account. Since the function model is linear with respect to the coefficients a_i, the fitting process employs a linear least-squares method, which does not require the definition of initialization values for their computation.

Also in the second case, a regression model parametric fitting approach has been employed. However, the function model selected assumes a rational form where both the numerator and the denominator are polynomials

$$\mathrm{rat}_{mn} : \; x = \frac{\sum_{i=0}^{m} a_i N^{m-i}}{N^n + \sum_{j=1}^{n} b_j N^{n-j}} \tag{4}$$

where a_i represents the coefficients of the polynomial of degree m at the numerator while b_j represents the coefficients of the polynomial of degree n at the denominator. Both indexes m and n can assume integer values in the range $[1, 5]$ and all the possible 25 m-n combinations have been considered. In addition, the coefficient of N^n is always unitary in order to have an unique combination of numerator and denominator in case their degrees are identical. Since the function model is not linear with respect to the coefficients a_i and b_j, the fitting process employs a non-linear least-squares method, which requires the definition of initialization values for their computation. However, despite based on the same dataset of sample points, different initialization values can produce diverse fitting curves. For this reason, in order to reduce the influence of the initialization values imposed during the fitting process, a brute force tuning approach has been used. Given the m-n rational model, the fitting process on the same dataset has been repeated for 1000 iterations, with the initialization values of the coefficients a_i and b_j randomly generated. Among the 1000 provided, the function that better matches the dataset has been considered as the rational fitting curve for the m-n combination. The same process has been executed for all the m-n combinations considered.

In the third case, a smoothing spline non-parametric approach has been employed. The definition of a smoothing parameter p determines the smoothness of the fitting curve. The parameter p can assume values between 0 (case of a straight line curve fit) and 1 (case of cubic spline interpolation curve). The function model assumes the form of piecewise polynomials. Consider partitioning the range in n intervals at $(n+1)$ breaking points $N_0, N_1, \ldots, N_n$

$$x = \begin{cases} \sum_{i=0}^{m} a_{i1} N^{m-i} & N_0 \le N \le N_1 \\ \vdots & \vdots \\ \sum_{i=0}^{m} a_{ik} N^{m-i} & N_{k-1} \le N \le N_k \\ \vdots & \vdots \\ \sum_{i=0}^{m} a_{in} N^{m-i} & N_{n-1} \le N \le N_n \end{cases} \tag{5}$$

[11] https://it.mathworks.com/help/curvefit/fit.html.

Table 6
Fitting curves (the best quality fitting curves for each model are highlighted).

Polynomial model			
Fit type	adj_{R^2}	$\mathrm{avg}_{\lvert err\rvert}$ [mm]	$\sigma_{\lvert err\rvert}$ [mm]
poly_1	0.9752	1.8932	1.3318
poly_2	0.9884	1.2434	0.9719
poly_3	0.9898	1.2035	0.8597
poly_4	0.9901	1.7799	0.8546
poly_6	0.9915	1.1114	0.7578
poly_7	**0.9923**	**1.0515**	**0.7355**
poly_8	0.9923	1.0499	0.7370
Rational model			
Fit type	adj_{R^2}	$\mathrm{avg}_{\lvert err\rvert}$ [mm]	$\sigma_{\lvert err\rvert}$ [mm]
rat_{11}	0.9751	1.8932	1.3318
rat_{12}	0.9894	1.2025	0.9142
rat_{13}	0.9899	1.1944	0.8601
rat_{14}	0.9917	1.1008	0.7458
rat_{15}	0.9922	1.0542	0.7401
rat_{21}	0.9884	1.2433	0.9721
rat_{22}	0.9898	1.1937	0.8688
rat_{34}	0.9933	0.9659	0.6979
rat_{35}	0.9933	0.9629	0.7003
rat_{44}	**0.9933**	**0.9616**	**0.7015**
Smoothing spline model			
p	adj_{R^2}	$\mathrm{avg}_{\lvert err\rvert}$ [mm]	$\sigma_{\lvert err\rvert}$ [mm]
0.00	0.9752	1.8932	1.3318
0.01	0.9921	1.0665	0.7445
0.02	0.9925	1.0354	0.7248
0.03	0.9927	1.0176	0.7175
0.05	0.9930	0.9948	0.7130
0.09	0.9932	0.9707	0.7109
0.20	0.9934	0.9578	0.6931
0.40	0.9935	0.9520	0.6816
0.51	0.9935	0.9495	0.6802
0.64	0.9935	0.9469	0.6800
0.73	**0.9935**	**0.9453**	**0.6804**
0.82	0.9935	0.9437	0.6813
0.93	0.9935	0.9415	0.6832
1.00	0.9935	0.9396	0.6855

where a_{ik} represents the coefficients of the kth polynomial piece. Each polynomial is of the third degree ($m = 3$). Several values of the smoothing parameter p have been investigated:

$$p = 0.01i \quad \text{with} \quad i = 0, \ldots, 100 \tag{6}$$

in order to evaluate its influence on the curves generated.

The fitting curve should provide a bijective relation between the number of phototransistors activated N and the distance x. For this reason, in every approach investigated only the fitting curves that present a strictly monotone trend have been considered as acceptable. Fig. 15 reports some examples of such curves for each one of the approaches investigated. For every instance, the upper graph shows the fitting curve with respect to the dataset of sample points while the lower graph illustrates the residuals of the fitting model.

The valid curves have been compared based on the adjusted R-square adj_{R^2} parameter, which gives an indication of the good quality of the fit. This parameter can assume values between 0 and 1: the closer to the unity, the more suitable the fitting model, since it provides a profile which follows better the variation of the data. Table 6 collects the curves for the three different function models. In addition to the corresponding adj_{R^2} parameter, for each curve the table reports the average $\mathrm{avg}_{\lvert err\rvert}$ and standard deviation $\sigma_{\lvert err\rvert}$ of the absolute of residuals, which provide an indication of the goodness of the fit. Considering the curves gathered, both the polynomial and the rational models present the whole set of valid curves. On the other hand, since in the case of the

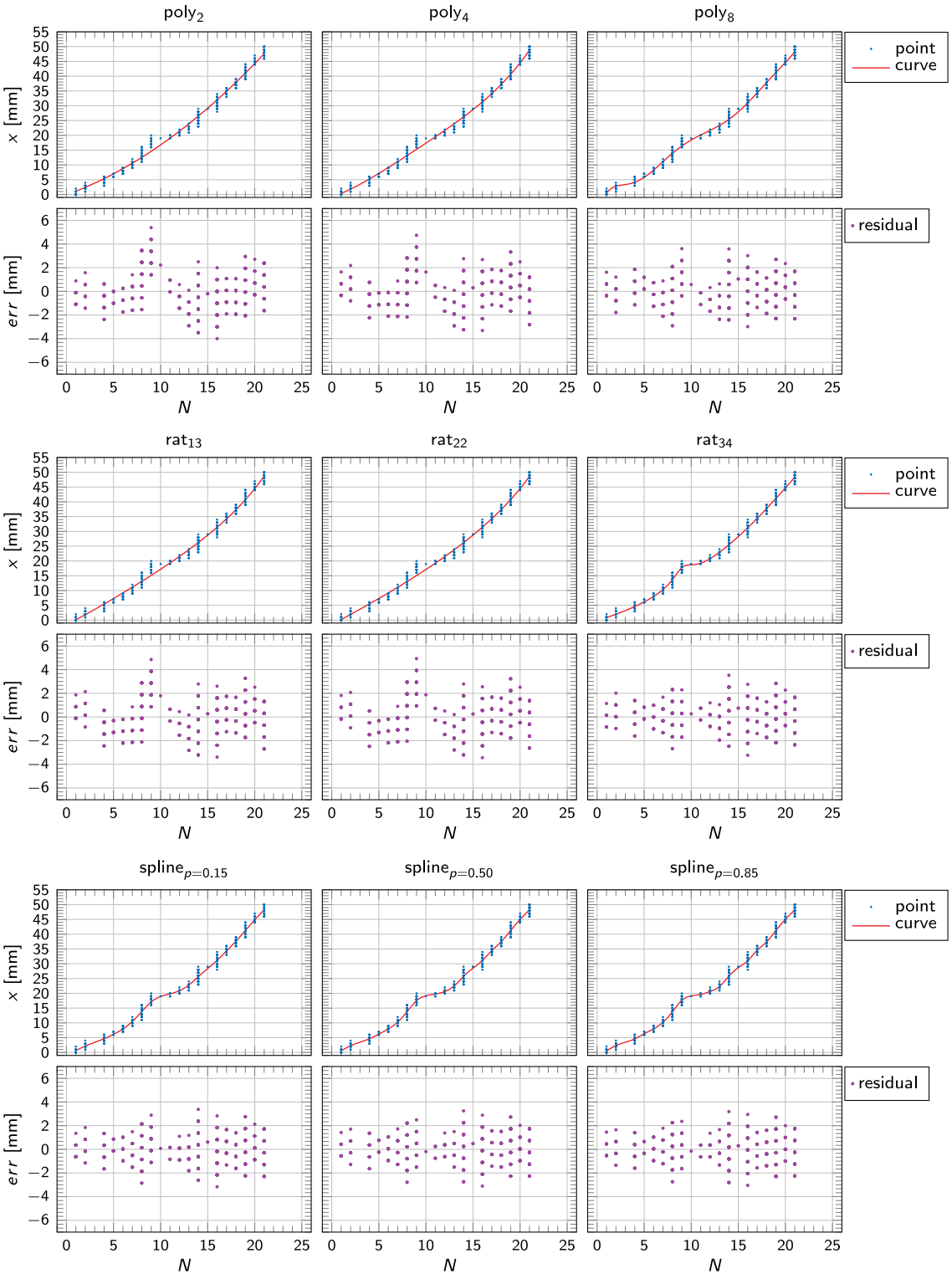

Fig. 15. Examples of fitting curves: polynomial model (poly_m); rational model (rat_{mn}) and smoothing spline model (spline_p). For each example, the upper graph reports the fitting curve with respect to the sample points, while the lower graph reports the residuals.

spline model the majority of fitting curves presents minor differences in terms of the parameter adj_{R^2}, only a selection of the valid ones is reported. Overall, the table shows how the curves that present a more suitable fitting profile (adj_{R^2} closer to unity) are characterized by a lower average value of absolute residuals. In this regard, in general the spline model tends to have greater values of adj_{R^2} compared to the other two models, thus describing better the variation of the dataset. However, given its piecewise structure, this enhanced flexibility is at the cost of a more complex function definition, requiring 17 different pieces for each function in the case of application, while both the polynomial and the rational models require a single function definition for the entire range considered.

The results highlighted in the table refer to the best fitting curves for each model. The selection procedure has been based on the closeness

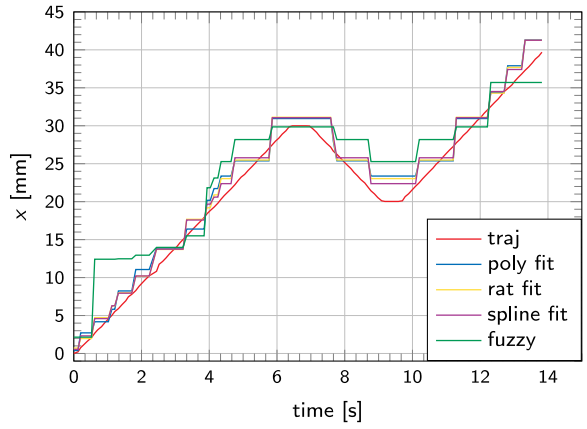

Fig. 16. Axial distance retrieval in the case of a continuous trajectory employing several approaches: polynomial fitting curve (*poly*); rational fitting curve (*rat*); spline fitting curve (*spline*); fuzzy logic inference system (*fuzzy*).

Table 7
Comparison between models for the axial distance retrieval in the case of a continuous trajectory.

Function model	$\text{avg}_{\lvert err \rvert}$ [mm]	$\sigma_{\lvert err \rvert}$ [mm]
poly_7	1.3911	1.3347
rat_{44}	1.3818	1.2473
$\text{spline}_{p=0.73}$	1.3573	1.1707
Fuzzy-logic	2.4498	2.7229

of the adjusted R-square adj_{R^2} parameter to the unity as main driver (for the sake of clarity, a limited number of significative digits has been reported in Table 6). These have been selected to be compared to each other and with the fuzzy-logic method in an application involving a continuous trajectory along the axial direction. The test procedure followed resembles the one described in Section 3.1.2. The in-plane matrix sensor has been placed on the fixed part of the rail while the infrared source has been mounted on the moving part. Keeping a condition of alignment between the LED and the centre of the sensor, a nominal continuous trajectory along the x axial direction has been imposed to the moving part of the slide. During the motion of the infrared source, the sensor provides the number of phototransistors activated N, information exploited by the methods to compute the axial distance. Fig. 16 illustrates the values of axial distances retrieved by each function employed with respect to the nominal trajectory. Table 7 reports the main results in terms of average and standard deviation of the absolute of errors as compared to the reference trajectory for each method. The table highlights how each fitting approach presents better performances as opposed to the fuzzy logic one. With reference to the fitting approaches, they present quite similar behaviours in terms of both mean error and error variance, with the spline curve approach being characterized by slightly lower values. Therefore, a trade-off among the fitting approaches, taking into account both performance and definition complexity as selection parameters, suggests how the rational curve seems the more suitable for the application case considered.

5. Conclusions

The work reported in this paper has been executed in the framework of the project AUTOMA, aimed at the development of technologies to enable both OOS, OOA, ADR operations by means of a robotic arm (orbital mission) and modular structure assembly operations by means of drones (planetary mission).

The design of the hardware involved, namely the capture interface and MAOU, has been described. The capture interface consists of a gripper mechanism and a suite of close-range navigation sensors (one navcam, four ToF, two custom matrices) in order to enable both the retrieval of the relative pose of the target and its capture. MAOU represents a unit aimed at the provision of the resources required by the target vehicle. Its structure has required the definition of interfaces to enable both its handling by means of the capture system and its docking with the target vehicle. A simplified mock-up version has been developed for laboratory evaluation.

The paper has mainly focused on the two custom matrix sensors embedded in the capture interface, namely the in-plane matrix and the roll matrix, with a detailed description of their design and the test campaign carried out for their characterization. With reference to the in plane-matrix, the sensor provides information about lateral displacement and axial distance of the target object with respect to the centre of the gripper mechanism with a resolution in the order of a few millimetres. The usage of a closing cap with tighter holes tends to slightly worsen the resolution of the sensor, both in axial and lateral directions. In terms of axial relative distance, both the use of tighter holes of the closing cap (on the sensor side) and a lower angular aperture of the beacon (on the source side) increase the range of application of the sensor. With reference to the roll matrix, the sensor provides information about the angular roll misalignment with respect to the axis of symmetry of the gripper mechanism with a resolution influenced by the distance from the target. In fact, an increase of the proximity corresponds to an improvement of the resolution. The best performance of 3.5 deg are for relative distances approximately up to 20 mm.

The last part of the paper has been dedicated to the definition of an analytical relation for the retrieval of the relative distance from the information provided by the in-plane matrix sensor. Three different approaches have been investigated: a polynomial fitting, a rational fitting and a spline fitting. The best curves of each model have been compared among them and with a fuzzy-logic approach in a continuous trajectory application. The tests have highlighted the better performances of the fitting approaches compared to the fuzzy logic one. In addition, these are characterized by quite similar behaviours, with the spline curve approach presenting slightly lower values in terms of mean error and variance error. However, taking into account both performance and definition complexity, the rational curve seems the more suitable for the application considered.

Declaration of competing interest

The authors declare that they have no known competing financial interests or personal relationships that could have appeared to influence the work reported in this paper.

Acknowledgements

This work was funded by the Department of Industrial Engineering of the University of Padua, Italy in the framework of the BIRD 2021 programme (BRAN-BIRD2121-01).

References

[1] A.M. Long, M.G. Richards, D.E. Hastings, On-orbit servicing: a new value proposition for satellite design and operation, J. Spacecr. Rockets 44 (4) (2007) 964–976, http://dx.doi.org/10.2514/1.27117.

[2] W.-J. Li, D.-Y. Cheng, X.-G. Liu, Y.-B. Wang, W.-H. Shi, Z.-X. Tang, F. Gao, F.-M. Zeng, H.-Y. Chai, W.-B. Luo, et al., On-orbit service (OOS) of spacecraft: A review of engineering developments, Prog. Aerosp. Sci. 108 (2019) 32–120, http://dx.doi.org/10.1016/j.paerosci.2019.01.004.

[3] C. Underwood, S. Pellegrino, V.J. Lappas, C.P. Bridges, J. Baker, Using CubeSat/micro-satellite technology to demonstrate the autonomous assembly of a reconfigurable space telescope (AAReST), Acta Astronaut. 114 (2015) 112–122, http://dx.doi.org/10.1016/j.actaastro.2015.04.008.

[4] M. Shan, J. Guo, E. Gill, Review and comparison of active space debris capturing and removal methods, Prog. Aerosp. Sci. 80 (2016) 18–32, http://dx.doi.org/10.1016/j.paerosci.2015.11.001.

[5] S. Eckersley, C. Saunders, D. Gooding, M. Sweeting, C. Whiting, M. Ferris, J. Friend, L. Forward, G. Aglietti, A. Nanjangud, et al., In-orbit assembly of large spacecraft using small spacecraft and innovative technologies, in: Proceedings of the 69th International Astronautical Congress, IAC, International Astronautical Federation (IAF), 2018.

[6] V. Cox, Companies demonstrate groundbreaking satellite life-extension service, 2020, https://news.northropgrumman.com/news/releases/northrop-grumman-successfully-completes-historic-first-docking-of-mission-extension-vehicle-with-intelsat-901-satellite (Accessed on 12/09/2023).

[7] K. Basham, Successful docking paves the way for future on-orbit and life-extension services through robotics, 2021, https://news.northropgrumman.com/news/releases/northrop-grumman-and-intelsat-make-history-with-docking-of-second-mission-extension-vehicle-to-extend-life-of-satellite (Accessed on 12/09/2023).

[8] J.L. Forshaw, G.S. Aglietti, S. Fellowes, T. Salmon, I. Retat, A. Hall, T. Chabot, A. Pisseloup, D. Tye, C. Bernal, et al., The active space debris removal mission RemoveDebris. Part 1: From concept to launch, Acta Astronaut. 168 (2020) 293–309, http://dx.doi.org/10.1016/j.actaastro.2019.09.002.

[9] G.S. Aglietti, B. Taylor, S. Fellowes, T. Salmon, I. Retat, A. Hall, T. Chabot, A. Pisseloup, C. Cox, A. Mafficini, et al., The active space debris removal mission RemoveDebris. Part 2: In orbit operations, Acta Astronaut. 168 (2020) 310–322, http://dx.doi.org/10.1016/j.actaastro.2019.09.001.

[10] C. Blackerby, A. Okamoto, K. Fujimoto, N. Okada, J.L. Forshaw, J. Auburn, ELSA-d: An in-orbit end-of-life demonstration mission, in: Proc. Int. Astronaut. Congr. IAC, Vol. 6, 2018, p. 43644.

[11] R. Biesbroek, S. Aziz, A. Wolahan, S. Cipolla, M. Richard-Noca, L. Piguet, The clearspace-1 mission: Esa and clearspace team up to remove debris, in: Proc. 8th Eur. Conf. Sp. Debris, 2021, pp. 1–3.

[12] S. Basu, T. Mast, G. Miyata, A proposed autonomously assembled space telescope (AAST), in: AIAA Space 2003 Conference & Exposition, 2003, p. 6369, http://dx.doi.org/10.2514/6.2003-6369.

[13] C. Underwood, S. Pellegrino, Autonomous assembly of a reconfigurable space telescope (AAReSt) for astronomy and Earth observation, in: 8th IAA Symposium on Small Satellites for Earth Observation, Berlin, 2011, pp. 4–8.

[14] N. Lee, P. Backes, J. Burdick, S. Pellegrino, C. Fuller, K. Hogstrom, B. Kennedy, J. Kim, R. Mukherjee, C. Seubert, et al., Architecture for in-space robotic assembly of a modular space telescope, J. Astron. Telesc. Instrum. Syst. 2 (4) (2016) 041207, http://dx.doi.org/10.1117/1.JATIS.2.4.041207.

[15] C. Saunders, D. Lobb, M. Sweeting, Y. Gao, Building large telescopes in orbit using small satellites, Acta Astronaut. 141 (2017) 183–195, http://dx.doi.org/10.1016/j.actaastro.2017.09.022.

[16] R. Gran, NASA's robotic OSAM-1 mission completes its critical design review, 2022, https://www.nasa.gov/feature/goddard/2022/nasa-s-robotic-osam-1-mission-completes-its-critical-design-review (Accessed on 12/09/2023).

[17] J. Harbaugh, On-Orbit servicing, assembly, and manufacturing 2 (OSAM-2), 2022, https://www.nasa.gov/mission_pages/tdm/osam-2.html (Accessed on 12/09/2023).

[18] L. Olivieri, A. Francesconi, Design and test of a semiandrogynous docking mechanism for small satellites, Acta Astronaut. 122 (2016) 219–230, http://dx.doi.org/10.1016/j.actaastro.2016.02.004.

[19] F. Branz, L. Olivieri, F. Sansone, A. Francesconi, Miniature docking mechanism for CubeSats, Acta Astronaut. 176 (2020) 510–519, http://dx.doi.org/10.1016/j.actaastro.2020.06.042.

[20] Z. Pavanello, F. Branz, A. Francesconi, A. Cenedese, R. Antonello, F. Basana, P. Iob, D. Vertuani, M. Massari, C. Colombo, et al., Combined control and navigation approach to the robotic capture of space vehicles, in: International Astronautical Congress: IAC Proceedings, 2021, pp. 1–13.

[21] F. Sansone, F. Branz, A. Francesconi, A relative navigation sensor for CubeSats based on LED fiducial markers, Acta Astronaut. 146 (2018) 206–215, http://dx.doi.org/10.1016/j.actaastro.2018.02.028.

[22] A. Caon, F. Branz, A. Francesconi, Development and test of a robotic arm for experiments on close proximity operations, Acta Astronaut. 195 (2022) 287–294, http://dx.doi.org/10.1016/j.actaastro.2022.03.006.

[23] A. Caon, F. Branz, A. Francesconi, Smart capture tool for space robots, Acta Astronaut. 210 (2023) 71–81, http://dx.doi.org/10.1016/j.actaastro.2023.05.014.

[24] A. Caon, M. Peruffo, F. Branz, A. Francesconi, Consensus sensor fusion to estimate the relative attitude during space capture operations, in: 2022 IEEE 9th International Workshop on Metrology for AeroSpace (MetroAeroSpace), IEEE, 2022, pp. 299–304, http://dx.doi.org/10.1109/MetroAeroSpace54187.2022.9856096.

[25] M. Imperatrice, A. Caon, M. Peruffo, F. Branz, A. Francesconi, Experimental campaign on the sensor package for a smart capture tool, in: 2023 IEEE 10th International Workshop on Metrology for AeroSpace (MetroAeroSpace), IEEE, 2023, http://dx.doi.org/10.1109/MetroAeroSpace57412.2023.10190000.

[26] A. Caon, F. Branz, A. Francesconi, Characterization of a new positioning sensor for space capture, in: 2021 IEEE 8th International Workshop on Metrology for AeroSpace (MetroAeroSpace), IEEE, 2021, pp. 424–429, http://dx.doi.org/10.1109/MetroAeroSpace51421.2021.9511704.